Icarus 264 (2016) 316–330

Contents lists available at ScienceDirect

Icarus

journal homepage: www.journals.elsevier.com/icarus

Fragment shapes in impact experiments ranging from cratering to catastrophic disruption

Tatsuhiro Michikami [a,*], Axel Hagermann [b], Tokiyuki Kadokawa [c], Akifumi Yoshida [a], Akira Shimada [c], Sunao Hasegawa [d], Akira Tsuchiyama [c]

[a] Faculty of Engineering, Kinki University, Hiroshima Campus, 1 Takaya Umenobe, Higashi-Hiroshima, Hiroshima 739-2116, Japan
[b] Department of Physical Sciences, The Open University, Walton Hall, Milton Keynes MK7 6AA, United Kingdom
[c] Division of Earth and Planetary Sciences, Graduate School of Science, Kyoto University, Kiashirakawa Oiwake-cho, Sakyo-ku, Kyoto 606-8052, Japan
[d] Institute of Space and Astronautical Science, Japan Aerospace Exploration Agency, Sagamihara, Kanagawa 252-8510, Japan

ARTICLE INFO

Article history:
Received 11 May 2015
Revised 20 September 2015
Accepted 23 September 2015
Available online 8 October 2015

Keyword:
Impact processes
Collisional physics
Asteroids
Asteroid Itokawa

ABSTRACT

Laboratory impact experiments have found that impact fragments tend to be elongated. Their shapes, as defined by axes *a*, *b* and *c*, these being the maximum dimensions of the fragment in three mutually orthogonal planes ($a \geqslant b \geqslant c$), are distributed around mean values of the axial ratios $b/a \sim 0.7$ and $c/a \sim 0.5$. This corresponds to $a{:}b{:}c$ in the simple proportion $2{:}\sqrt{2}{:}1$. The shape distributions of some boulders on Asteroid Eros, the small- and fast-rotating asteroids (diameter <200 m and rotation period <1 h), and asteroids in young families, are similar to those of laboratory fragments created in catastrophic disruptions. Catastrophic disruption is, however, a process that is different from impact cratering. In order to systematically investigate the shapes of fragments in the range from impact cratering to catastrophic disruption, impact experiments for basalt targets 5–15 cm in size were performed. A total of 28 impact experiments were carried out by firing a spherical nylon projectile (diameter 7.14 mm) perpendicularly into the target surface at velocities of 1.60–7.13 km/s. More than 12,700 fragments with $b \geqslant 4$ mm generated in the impact experiments were measured. We found that the mean value of c/a in each impact decreases with decreasing impact energy per unit target mass. For instance, the mean value of c/a in an impact cratering event is nearly 0.2, which is considerably smaller than c/a in a catastrophic disruption ($\sim$0.5). The data presented here can provide important evidence to interpret the shapes of asteroids and boulders on asteroid surfaces, and can constrain current interpretations of asteroid formation. As an example, by applying our experimental results to the boulder shapes on Asteroid Itokawa's surface, we can infer that Itokawa's parent body must have experienced a catastrophic disruption.

1. Introduction

In laboratory impact experiments, the shapes of fragments from catastrophic collisions defined by axes *a, b* and *c*, these being the maximum dimensions of the fragment in three mutually orthogonal planes ($a \geqslant b \geqslant c$), have been found to behave in a very regular way (see the pioneering work of Fujiwara et al., 1978). The axial ratios are distributed around mean values of the axial ratios $b/a \sim 0.7$ and $c/a \sim 0.5$, i.e. corresponding to $a{:}b{:}c$ in the simple proportion $2{:}\sqrt{2}{:}1$. The data indicate a general property of collisional fragments, which is repeated with great regularity in widely different experimental conditions such as projectile velocity, target shape, composition and strength (Fujiwara et al., 1978; Matsui et al., 1982, 1984; Bianchi et al., 1984; Capaccioni et al., 1984, 1986; Durda et al., 2015).

The shape distributions of small asteroids less than tens of kilometers in diameter are considered to be similar to distributions obtained for fragments generated in laboratory impact experiments (Fujiwara et al., 1978; Capaccioni et al., 1984, 1986). The shapes of most asteroids can be inferred from the observed light curve amplitude. For instance, Szabó and Kiss (2008) have determined the shape distribution of 11,735 asteroids based on the Sloan Digital Sky Survey Moving Object Catalog. In particular, they have researched eight prominent asteroid families. Nearly one-third of all asteroids belong to families (Zappalà et al., 1995) that are believed to be a result of collisional disruption of parent asteroids (O'Brien and Greenberg, 2005). In young families, the shape distributions of asteroids are very similar to the distributions obtained for fragments generated in laboratory impact

* Corresponding author.
E-mail address: michikami@hiro.kindai.ac.jp (T. Michikami).

http://dx.doi.org/10.1016/j.icarus.2015.09.038
0019-1035/

experiments. In old asteroid families, on the other hand, the shape distributions of asteroids are more spherical as impact-related phenomena occur (impact reshaping and impact-induced seismic activity are dominant processes in the late evolution of asteroid shapes). The shapes of larger asteroids are also more spherical due to self-gravitational effects (e.g., Capaccioni et al., 1984).

Michikami et al. (2010) investigated the shapes of boulders with sizes of 0.1–220 m on Asteroid 433 Eros using a few arbitrarily selected images taken by the NEAR spacecraft. Moreover, the shapes of small and fast-rotating asteroids (diameter < 200 m and rotation period < 1 h), which are natural fragments from previous impact events among asteroids, were inferred from archived light curve data taken by ground-based telescopes. The results show that the shape distributions of laboratory fragments are similar to those of the boulders on Eros and of the small and fast-rotating asteroids. One has to bear in mind, however, that almost all of the data about fragment shapes in the laboratory were obtained from catastrophic disruption.

The shapes of fragments in non-catastrophic disruption such as impact cratering would be different from those in catastrophic disruption (e.g., Lange and Ahrens, 1981) because the strength of the shock wave in the target is relatively weak and only the surface of the target is broken. Lange and Ahrens (1981) carried out impact experiments for water ice targets (at temperatures of 81 K and 257 K) in order to investigate the correlation among the shape of fragments, temperature and the degree of fragmentation (cratering, erosion, disruption, and total fragmentation). Their results show that the shapes of fragments in a weak disruption at 257 K are different from those in a catastrophic disruption. Therefore, the shapes of fragments are considered to reflect the degree of fragmentation of the target.

Although the experiment of Lange and Ahrens (1981) is the only laboratory experiment to research the shapes of fragments from non-catastrophic to catastrophic disruption, the data currently available are not sufficient to develop a comprehensive model that includes impact phenomena among asteroids. This is mainly for the following three reasons.

(1) Because Lange and Ahrens' study focused on the collisional interaction of icy planetary bodies, the impact velocities in the experiments are low (0.14–1 km/s) compared with the average impact velocity (~5 km/s) in the asteroid main belt. Of course, the dynamic disruption of silicate bodies is also different from those of icy bodies.
(2) Unfortunately, the data of the fragment shapes in impact cratering were not shown, although Lange and Ahrens carried out the impact experiments in the entire range from impact cratering to catastrophic disruption. As a reason, we think that the total number of fragments counted in impact cratering is very small, because in each shot only very few (several tens of) fragments were counted. In general, for the impact experiments using targets of similar size, fewer fragments are produced in impact cratering than in heavier disruptions.
(3) The shapes of fragments in the case of weak disruption (non-catastrophic disruption) are different in 257 K and 81 K ice targets. The fragment shapes in 81 K ice targets are similar to those for catastrophic disruption of basalt targets, and are independent of the degree of fragmentation. On the other hand, the shapes of fragments in 257 K ice targets depend on the degree of fragmentation. That is, in the case of 257 K ice targets, the shapes of fragments in a strong (catastrophic) disruption are similar to those for catastrophic disruption of basalt targets, while those in a weak disruption (many plate-like shaped fragments are seen) are different from those for a catastrophic disruption of basalt targets. The difference of the results in 81 and 257 K targets may be (according to the suggestion of the authors) due to the fact that it is difficult to produce the 81 K targets without numerous cracks and air bubbles. Lange and Ahrens (1981) pointed out that the growth rate in 81 K ice was much faster than that in 257 K ice, thus causing the 81 K targets to contain significantly more cracks and air bubbles. Indeed, their 81 K ice targets were much weaker than the 257 K ice targets. These cracks and air bubbles would affect the resulting shapes of the fragments. Therefore, we are confident that only a comparison of the data of 257 K ice targets with our experimental data is meaningful.

In this study, in order to investigate the shapes of fragments in the entire range from impact cratering to catastrophic disruption, impact experiments into silicate (basalt) targets with various sizes were carried out. The research described here is intended to constrain current interpretations of asteroid formation.

2. Experimental method

2.1. Target properties

The samples used as targets were fine-grained and very homogeneous basalts from Linxi, Inner Mongolia. The optical microscopic image of a thin section of the basalt is shown in Fig. 1a. The lath-like crystals are micro-phenocrysts plagioclase and their

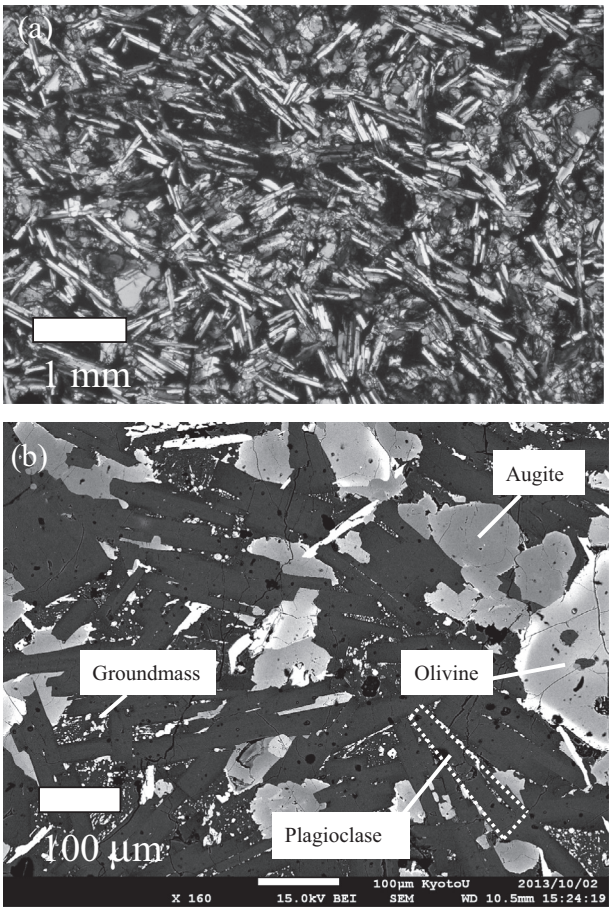

Fig. 1. Microscopic images of the basalt samples used as targets. (a) Optical microscope image of a thin section in crossed polarized light. (b) SEM back scattered electron image of the thin section.

lengths are from several hundred micrometers to one millimeter. Several tens of olivine and augite crystals can be also seen in the glassy groundmass (dark areas). Fig. 1b shows the scanning electron microscopic (SEM) image of the thin section. The interstitial areas between plagioclase, olivine and augite crystals are the groundmass composed of glass and fine mineral grains.

The target bulk density is 3000 kg/m^3, the compressive strength is 185 MPa, and the tensile strength is 14 MPa (obtained from a cylinder splitting test). The compressive strength is similar to the values of basalts used in previous experiments such as those by Fujiwara et al. (1977) (160 MPa) and Matsui et al. (1982) (220 MPa). Besides, the strength of basalt targets used in the experiments is very similar to that of ordinary chondrites. For instance, the compressive and the tensile strengths of LL3 chondrite Krimka are 160 MPa and 22 MPa, respectively (Medvedev et al., 1985). Thus, our basalt targets are no less appropriate as mechanical analogs for asteroids than the materials used in previous experiments.

2.2. Impact experiments

The 28 impact experiments for basalts with several shapes were accomplished with a two-stage light-gas gun at the Institute of Space and Astronautical Science, Japan Aerospace Exploration Agency (ISAS, JAXA). In all runs, spherical nylon projectiles 7.14 mm in diameter (mass 0.217 g and density 1140 kg/m^3) were shot perpendicularly into the target surface. The impact velocities of the projectiles ranged from 1.60 to 7.13 km/s keeping projectile mass constant.

In many shots, cubic targets were used, just as in the experiments of Fujiwara et al. (1977, 1978). We carried out three types of impact experiments as follows.

(1) Four experiments (s2127, s2133, s2134 and s2415) were carried out under nearly identical conditions to confirm the reproducibility of the experimental results. In these experiments, projectiles were shot at cubic targets with 5 cm side length at impact velocities of ~3.7 km/s.
(2) In order to cover a relatively wide range of scenarios from impact cratering to catastrophic disruption, we carried out impact experiments for four types of cubic targets with 5 cm, 7.5 cm, 10 cm, and 15 cm side length. As an indicator of target fragmentation, a specific energy, Q, which is defined as the kinetic energy of the projectile per unit target mass, is a widely used measure in such laboratory studies and numerical simulations (e.g., Holsapple et al., 2002). In the present paper, Q varied by two orders of magnitude (150–~15,000 J/kg). In this wide range of Q values, the impact experiments were carried out changing the impact velocities and the target sizes.
(3) In order to investigate the effect of target shape on fragment shape, we conducted impact experiments on spherical, rectangular parallelepiped (2:1:1 side ratio) and slab (10:10:1 side ratio) targets with the same mass as our cubic target with 5 cm side length. Impact velocities were approximately 3.5 km/s. We used a total of five targets that were not cubical (one sphere, two rectangular parallelepipeds and two slab targets). Target size (and shape) and impact conditions are summarized in Table 1.

Each target was set on a cylindrical stand less than one third of the target size in diameter. The accuracy of the position of the target from the muzzle of the gun was within 3 mm. The whole system was mounted in a vacuum chamber (nearly 1 × 1 × 2 m^3) with

Table 1
Target properties and the experimental results. M_t, M_l and Q are initial target mass, largest fragment mass and specific energy, respectively. Fragmentation types are cratering (Type I), transition type (Type II), core type (Type III) and complete destruction (Type IV). The mass and shapes of the fragments with $b \geqslant 4$ mm are measured. As exceptions, in s2132, s2137, s2570 and s2572, the counted fragments and the mean values of b/a and c/a do not contain the largest fragment whose mass is roughly the same as initial target mass. In the experiments, mass recovery refers to the mass ratio of fragments measured ($b \geqslant 4$ mm) to the initial target.

Shot number	Target shape	Dimension (cm)	M_t (g)	Impact features				Fragments			
				Velocity (km/s)	Q (J/kg)	Fragmentation type	M_l/M_t	Mean value of b/a	Mean value of c/a	Counted number ($b \geqslant 4$ mm)	Mass recovery ($b \geqslant 4$ mm) (%)
s1934	Cube	15 × 15 × 15	10149.0	6.87	500	II	0.778	0.70	0.33	468	99
s2126	Cube	7.5 × 7.5 × 7.5	1240.4	6.99	4280	III	0.051	0.71	0.41	1659	76
s2127	Cube	5 × 5 × 5	367.6	3.66	3960	III	0.096	0.73	0.47	541	78
s2128	Cube	7.5 × 7.5 × 7.5	1240.7	3.69	1190	III	0.410	0.69	0.39	338	97
s2129	Cube	5 × 5 × 5	360.9	5.32	8540	IV	0.018	0.74	0.45	756	49
s2130	Cube	7.5 × 7.5 × 7.5	1227.1	5.27	2470	III	0.088	0.71	0.41	1194	88
s2131	Cube	10 × 10 × 10	2948.9	5.32	1050	III	0.211	0.71	0.38	686	98
s2132	Cube	7.5 × 7.5 × 7.5	1229.9	1.60	230	I	0.999	0.69	0.24	5	100
s2133	Cube	5 × 5 × 5	363.5	3.63	3950	III	0.063	0.74	0.46	602	75
s2134	Cube	5 × 5 × 5	364.0	3.87	4490	III	0.049	0.74	0.45	618	75
s2135	Sphere	6.2	385.4	3.87	4240	III	0.208	0.75	0.45	604	82
s2137	Cube	7.5 × 7.5 × 7.5	1239.7	2.10	390	II	0.961	0.68	0.28	14	100
s2414	Cube	5 × 5 × 5	361.7	4.05	4930	III	0.280	0.70	0.42	166	92
s2415	Cube	5 × 5 × 5	368.1	3.71	4050	III	0.068	0.73	0.44	489	82
s2416	Cube	5 × 5 × 5	365.0	2.07	1270	III	0.205	0.73	0.44	105	98
s2417	Cube	5 × 5 × 5	366.1	7.13	15,060	IV	0.008	0.74	0.43	762	36
s2420	Cube	5 × 5 × 5	347.5	1.83	1040	II	0.733	0.73	0.43	47	99
s2421	Parallelepiped	6.3 × 6.3 × 3.15	341.9	3.41	3690	III	0.029	0.74	0.46	522	88
s2422	Slab	10.8 × 10.8 × 1.08	363.8	3.30	3240	III	0.117	0.70	0.36	232	94
s2423	Cube	7.5 × 7.5 × 7.5	1168.1	3.61	1210	III	0.155	0.72	0.40	269	95
s2568	Parallelepiped	6.3 × 6.3 × 3.15	339.4	3.20	3270	III	0.105	0.70	0.43	290	87
s2569	Slab	10.8 × 10.8 × 1.08	357.7	3.58	3880	III	0.546	0.66	0.35	94	98
s2570	Cube	15 × 15 × 15	10031.0	5.01	270	II	0.944	0.71	0.26	118	100
s2572	Cube	15 × 15 × 15	10058.0	3.72	150	I	0.997	0.66	0.17	23	100
s2574	Cube	5 × 5 × 5	355.9	3.10	2930	III	0.059	0.73	0.44	341	97
s2575	Cube	10 × 10 × 10	2923.7	6.98	1820	III	0.212	0.71	0.38	1419	94
s2576	Cube	10 × 10 × 10	2930.2	3.78	530	II	0.836	0.73	0.34	112	99
s2578	Cube	5 × 5 × 5	359.4	2.76	2310	III	0.072	0.73	0.46	302	93

acrylic resin windows. The ambient pressure in the chamber was less than 200 Pa.

The experiments were carried out with two different experimental setups. In the first setup (from shot s1934 to s2137), two high-speed framing cameras were oriented to view the collisional breakup through the side and top windows of the chamber. The fields of view of the two cameras were approximately 25×15 cm^2 (side camera) and 30×20 cm^2 (top camera), respectively. The framing rate of the camera was set to 4000 frames/s. Fragments with enough kinetic energy may break again when they hit the interior surface of the chamber. To prevent the destruction of fast fragments by secondary collisions, three styrofoam boards 1 cm thick were therefore put on the interior of the chamber. One ($\sim 30 \times 30$ cm^2) was put on the cylindrical stand's feet (near the impact point), the second one ($\sim 42 \times 30$ cm^2) was put on the floor of the chamber in front of the impact side (i.e. in the direction of the gun muzzle), and the third one (70×42 cm^2) was put on the chamber wall with the entrance hole for the projectile (the gun muzzle's direction).

In the second setup (from shot s2414 to s2578), a cardboard box ($59 \times 56 \times 45$ cm^3) whose interior was covered with 1 cm thick urethane sheets was put on the floor of the chamber, and each target was set in this box to effectively prevent destruction by secondary collisions of most fragments. The ambient pressure in the box was the same as before. The box has a vinyl sheet window. A high-speed framing camera was oriented to view the collisional breakup only through the vinyl sheet window that connects to the side window of the chamber. No pictures were taken through the top window of the chamber. Otherwise, the shot conditions were the same as before. In the experiments, the high-speed framing camera was used to investigate the behavior of the fragments and to confirm that destruction by secondary collisions had been prevented.

3. Results

3.1. Degree of fragmentation

In the experiments, the degrees of fragmentation of the target are grouped into four types in the order of decreasing Q:

Type I, cratering with no catastrophic disruption [$Q < 250$ J/kg].
Type II, a transition type where parts of the side surfaces are chipped off [$250 \leqslant Q < 1050$ J/kg].
Type III, the so-called core type, which is signified by whole surfaces of the target being spalled off with only the core in the central part of the target remaining [$1050 \leqslant Q < 8000$ J/kg].
Type IV, complete destruction, in which the targets are completely destroyed into fine fragments and no core is left [8000 J/kg $\leqslant Q$].

The type of each shot is shown in Table 1. The thresholds of Q dividing our experiments into four types are compatible with the experiments of Fujiwara et al. (1977), who carried out similar impact experiments on cubic basalt targets with sizes from about 2 to 10 cm at an impact velocity of 2.6 km/s in order to investigate the size distribution of the fragments.

The ratio of the mass of the largest fragment to the initial target mass (M_l/M_t) is a useful parameter to denote the degree of fragmentation of the target in a wide range of experimental conditions. M_l/M_t is large when impact cratering occurs, and is small when catastrophic disruption occurs. Fig. 2 shows the M_l/M_t ratio, as a function of the specific energy Q for our own experiments as well as earlier ones. The data show that the degree of fragmentation is dependent on the target material. M_l/M_t decreases with increasing Q, and there is a power-law relationship between M_l/M_t and Q in the same material type. The scatter within the same material type is related to the differences in target strength, impact velocity, projectile types, temperature, and other factors. Our data are similar to previous data of basalts, confirming a good reproducibility of the experimental results.

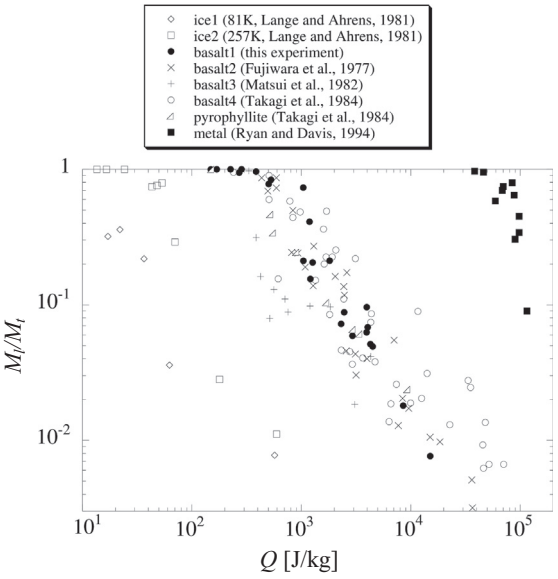

Fig. 2. Comparison of our own and previous experimental results for the M_l/M_t ratios, as a function of the specific energy Q, where M_l is the largest fragment mass, M_t is the initial target mass, and Q is the kinetic energy of the projectile per unit target mass. The data of two rectangular parallelepipeds and slab targets in our experiments were excluded because their shapes were different for a meaningful comparison. (See above-mentioned references for further information.)

3.2. Fragment shapes

After the impact, all fragments in the chamber were collected. We tried to collect as many fragments as possible, and the shapes and masses of fragments with $b \geqslant 4$ mm were individually measured. In the present study, fragment shape is defined by the ratios b/a and c/a, where a, b and c are defined as the dimensions of a fragment in three mutually orthogonal planes ($a \geqslant b \geqslant c$). We started by measuring the shortest dimension of the fragment, and then the shortest dimension perpendicular to this and, finally, the dimension perpendicular to both. The dimensions were measured with digital calipers. The errors in fragment lengths are accurate within ±0.01 mm. The numbers of fragments measured for individual experiments are from 5 to 1659 (Table 1). Overall, more than 12,700 fragments were measured. In the following subsections, we will describe (1) the reproducibility of the experimental results, (2) the relation between degree of fragmentation and fragment shapes, and (3) the relation between target shapes and fragment shapes.

3.2.1. Reproducibility of the experimental results

Fig. 3 shows the histogram of b/a and c/a (s2127, s2133, s2134 and s2415) with $b \geqslant 4$ mm obtained from the impact experiments under almost identical conditions (cubic target with 5 cm side length and impact velocity ~ 3.7 km/s). The mean b/a and c/a ratios in these experiments are similar, about 0.74 and 0.46, respectively. The shape distributions are also similar. In other words, most of fragments lie in the region of the histogram defined by $b/a > 0.4$ and $c/a > 0.2$, and the peaks of the histograms in the axial ratios of b/a and c/a are the same except for the c/a peak in s2415. In

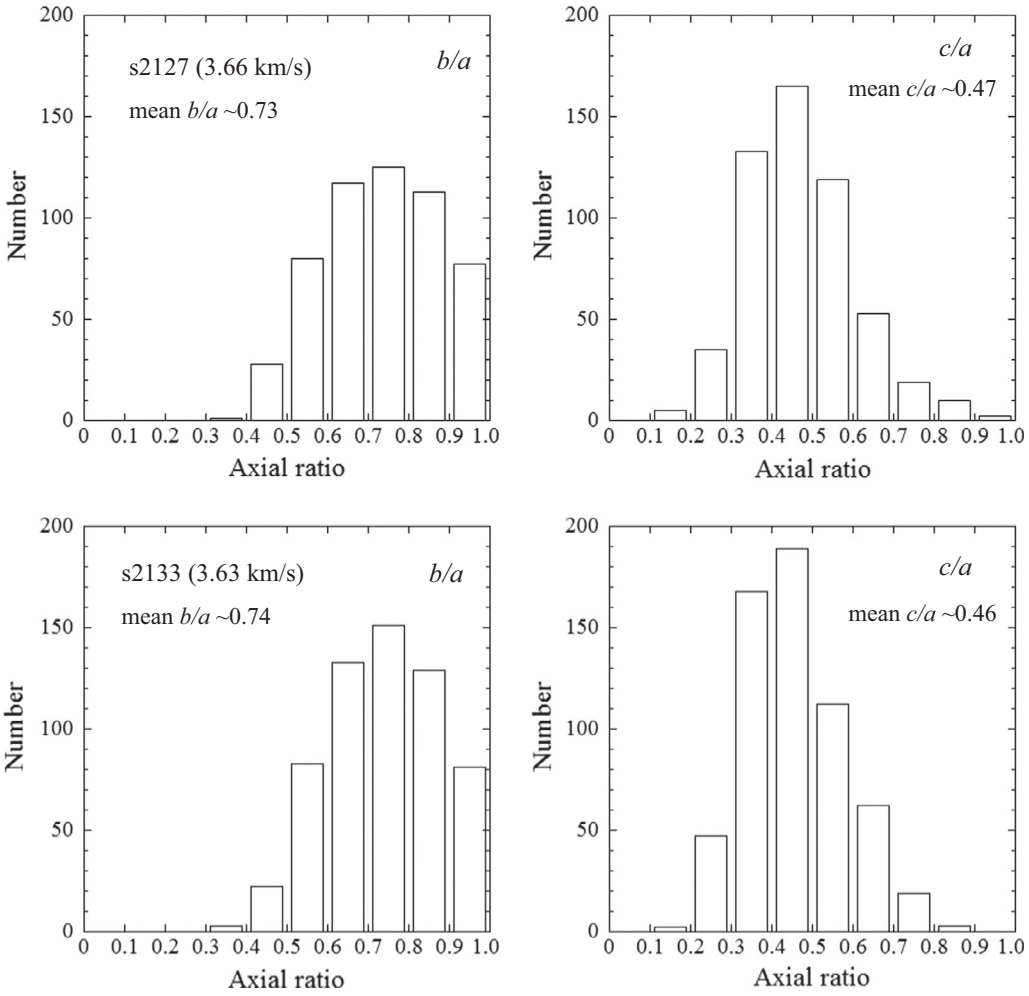

Fig. 3. Histograms of b/a and c/a (s2127, s2133, s2134 and s2415) with $b \geqslant 4$ mm obtained from the impact experiments under almost identical conditions (cubic target with 5 cm side length and impact velocity ~ 3.7 km/s). Impact velocities and mean b/a and c/a ratios are indicated.

these experiments, the shape distributions are similar to those reported by Fujiwara et al. (1978) and Capaccioni et al. (1984). In addition to the shape distributions of the fragments, the mass distributions of the fragments are also important results to confirm the reproducibility of the experimental results. The fragment mass distributions for four experiments presented in Fig. 3 are also very similar (see Fig. 4). Therefore, since the shape and mass distributions of the fragments are very similar, the reproducibility of the experimental results is considered to be good.

3.2.2. Degree of fragmentation and fragment shapes

To investigate the relation between the degree of fragmentation and the fragment shapes, the 23 impact experiments for cubic targets with 5–15 cm side length were carried out. As an example of these impact experiments, a typical diagram of b/a and c/a is shown in Fig. 5. The impact velocity was approximately maintained (~5 km/s) whilst the target size was changed from 5 cm to 15 cm side length (s2129, s2130, s2131 and s2570), with the exception of shot s2572, where the impact velocity was 3.72 km/s and target size was 15 cm side length. The impact velocities of ~5 km/s correspond to the mean collisional velocity among the main belt asteroids. Shot s2129 is of Type IV (complete destruction), s2130 and s2131 are Type III (core type), and s2570 is Type II (transition type). Fragmentation of Type I (impact cratering) was not observed in the experiments with an impact velocity of ~5 km/s because the maximum target size is 15 cm. Thus, as an example of the impact experiments of Type I, the data of s2572 with impact velocity of 3.72 km/s were added to these experimental data. In our experiments, we did not observe any extreme fragment shapes such as spheres, plates and bars, as reported by Fujiwara et al. (1978) for their experiments.

In Fig. 5, the shapes of fragments seem to differ by the degree of fragmentation. Fig. 6 shows the histogram of b/a and c/a for the experiments of Fig. 5. In Type IV impacts, almost all the fragments lie in the region of the diagram (histogram) defined by $b/a > 0.3$ and $c/a > 0.2$, which are similar to previous experimental data (e.g., Fujiwara et al., 1978; Capaccioni et al., 1984, 1986). However, in Type III, II and I impacts, the number of fragments in the region of the histogram by $c/a \leqslant 0.2$ slightly increases, decreasing with the degree of fragmentation (i.e. decreasing with the specific energy, Q). Note that this trend has not been found in previous experiments, except for the 257 K ice targets of Lange and Ahrens (1981). The peaks of the histograms in the axial ratio of c/a shift to small values in the case of small degrees of fragmentation. On the other hand, the peaks in the axial ratio of b/a seem to be constant regardless of the degree of fragmentation. Those trends are independent of the fragment mass (see Appendix A). In previous experiments, the mean c/a ratios were no less than 0.3 because these experimental data were obtained mainly from catastrophic disruption.

It is important to note that the fragment mass distribution can be used to denote the degree of fragmentation of the target. Fig. 7

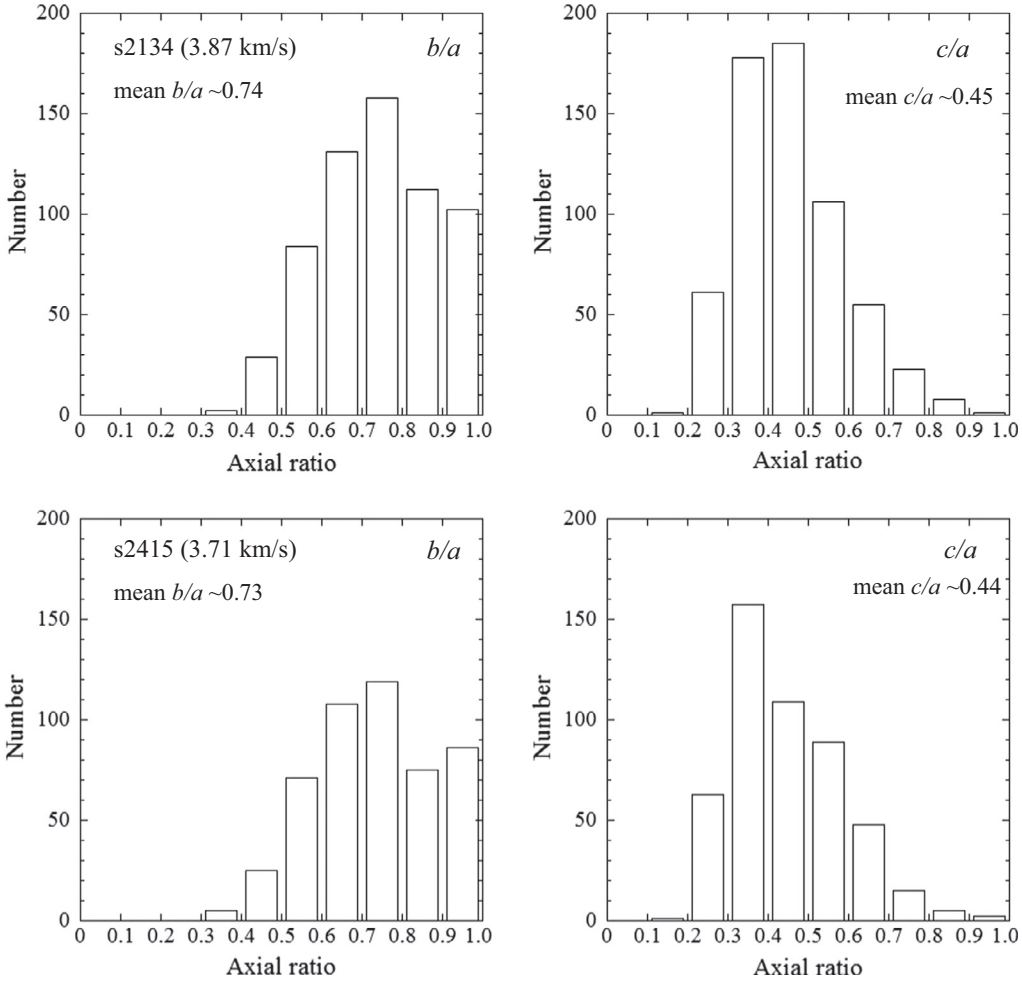

Fig. 3 (*continued*)

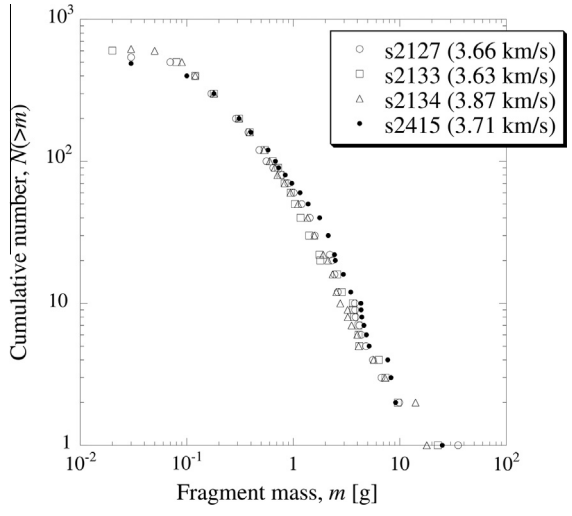

Fig. 4. Mass distributions of fragments for the experiments shown in Fig. 3 (s2127, s2133, s2134 and s2415). The horizontal and the vertical axes show the masses of the fragments and the cumulative number of fragments with a mass greater than m, respectively. The collection ratios of the total mass of fragments with $b \geqslant 4$ mm to the initial target mass are nearly 80% under these conditions while the recovery ratios of the total mass of all collected fragments (containing small fragments with $b < 4$ mm) to the initial target mass are more than 90%. The impact velocity of each shot is given in parentheses. The standard deviations of the distributions are similar (0.12–0.15).

shows the mass distribution for the experiments presented in Figs. 5 and 6. The mass distributions of fragments are represented by power laws. The value of the exponent in the power law distribution depends on the degree of fragmentation of the target. The heavier the degree of fragmentation, the higher the exponent becomes (i.e. the amount of small fragments increases). As shown in Fig. 7, for small fragments with less than 10 g, the values of the exponents range from 0.4 to 1.1 (in response to increasing Q). For other experiments on cubic targets, the values of the exponents for small fragments do not differ much from these values. The values in our experiments are compatible with previous experimental data for basalt targets (e.g., Fujiwara et al., 1977; Takagi et al., 1984).

Comparing the shape and the mass distributions of the fragments, the exponent of the mass distribution does not seem to affect the shape distribution. For example, the mean c/a ratios for s2131 and s2570 are different although the exponent values for small fragments with less than 10 g are the same (0.5). The same tendency was seen for other experiments. Thus, we could not find a relation between the exponent values in mass distributions and fragment shapes.

The tendency for the mean c/a ratios to decrease in the case of weak disruption was also found from our other experiments with impact velocities of 1.60–7.13 km/s. In order to investigate the relation between the fragment shape and the degree of the fragmentation, the mean axial ratios are plotted against Q (Fig. 8). Fig. 8 indicates that the mean b/a ratios seem to be roughly

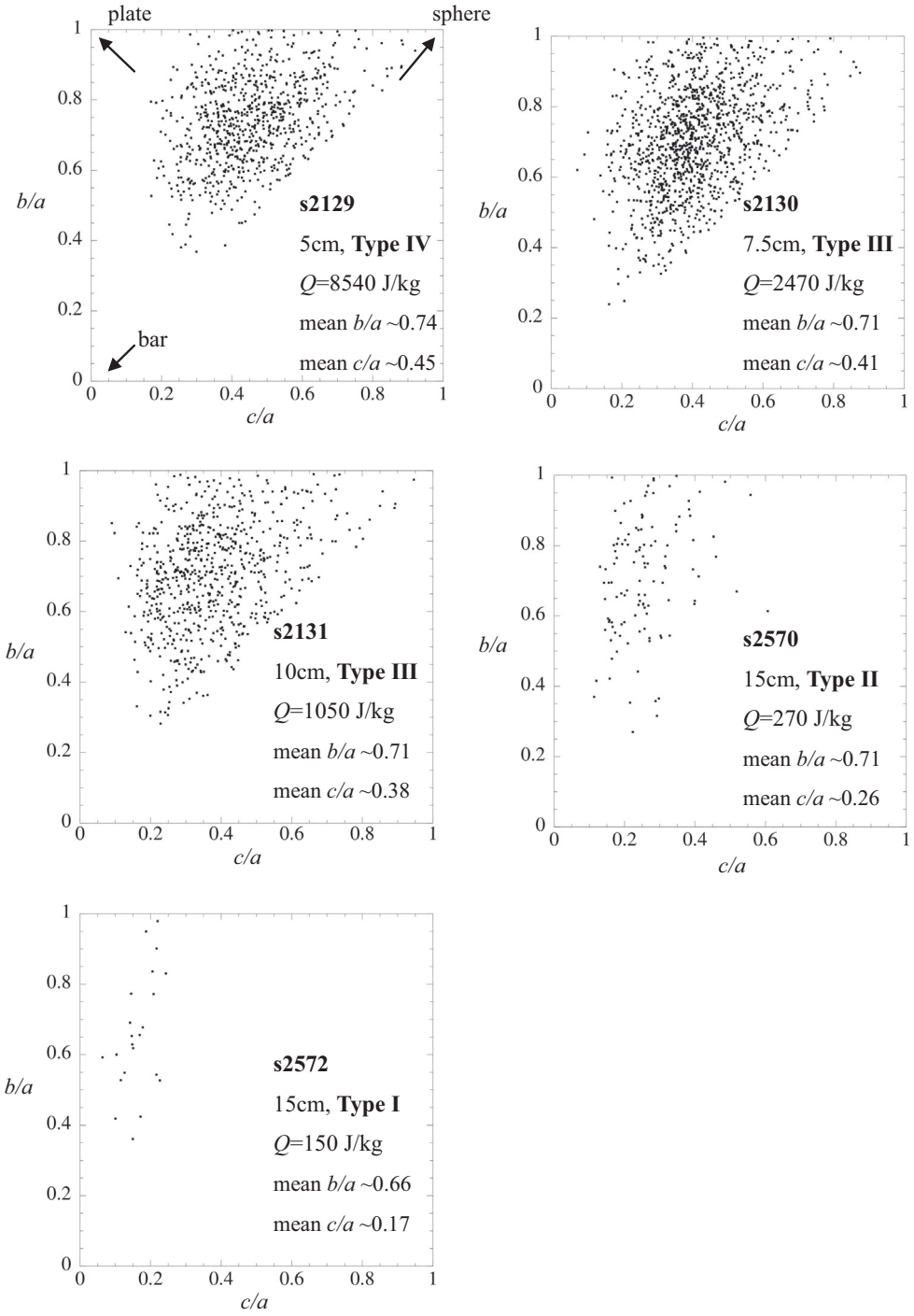

Fig. 5. A typical diagram for the shape distributions of fragments with $b \geqslant 4$ mm obtained from the cubic targets. These data are obtained by keeping approximately same impact velocity (~5 km/s) with changing target size of 5–15 cm side length (s2129, s2130, s2131 and s2570), except for shot s2572, where the impact velocity was 3.72 km/s and the target size was 15 cm side length. Target sizes, fragmentation types, values of Q and mean b/a and c/a ratios are indicated. The impact velocities are 5.32 km/s (s2129), 5.27 km/s (s2130), 5.32 km/s (s2131), 5.01 km/s (s2570) and 3.72 km/s (s2572), respectively. In s2570 and s2572, the mean b/a and c/a ratios do not contain the largest fragment whose mass is roughly the same as initial target mass.

constant, or seem to slightly decrease with decreasing Q. On the other hand, although the mean c/a ratios seem to be roughly constant when $Q \geqslant 1000$ J/kg, they decrease gradually with decreasing Q when $Q < 1000$ J/kg (From another point of view, the small c/a values are acquired from relatively large targets with 10 and 15 cm side length, and partly from targets with 7.5 cm side length. For identical Q, the mean c/a (and b/a) ratios in larger targets are slightly smaller than those in smaller ones). This means that there are more flat fragments in impact types I and II. We note that this trend has not been found in previous experiments. For instance, the mean c/a ratio (s2572) in impact cratering is 0.17, which is significantly less than in previous experiments. We therefore find that the mean c/a ratios strongly depend on Q, and not on target size or impact velocity. The fragment shapes in catastrophic disruption (Types III and IV) are obviously different from those in non-catastrophic disruption (Types I and II).

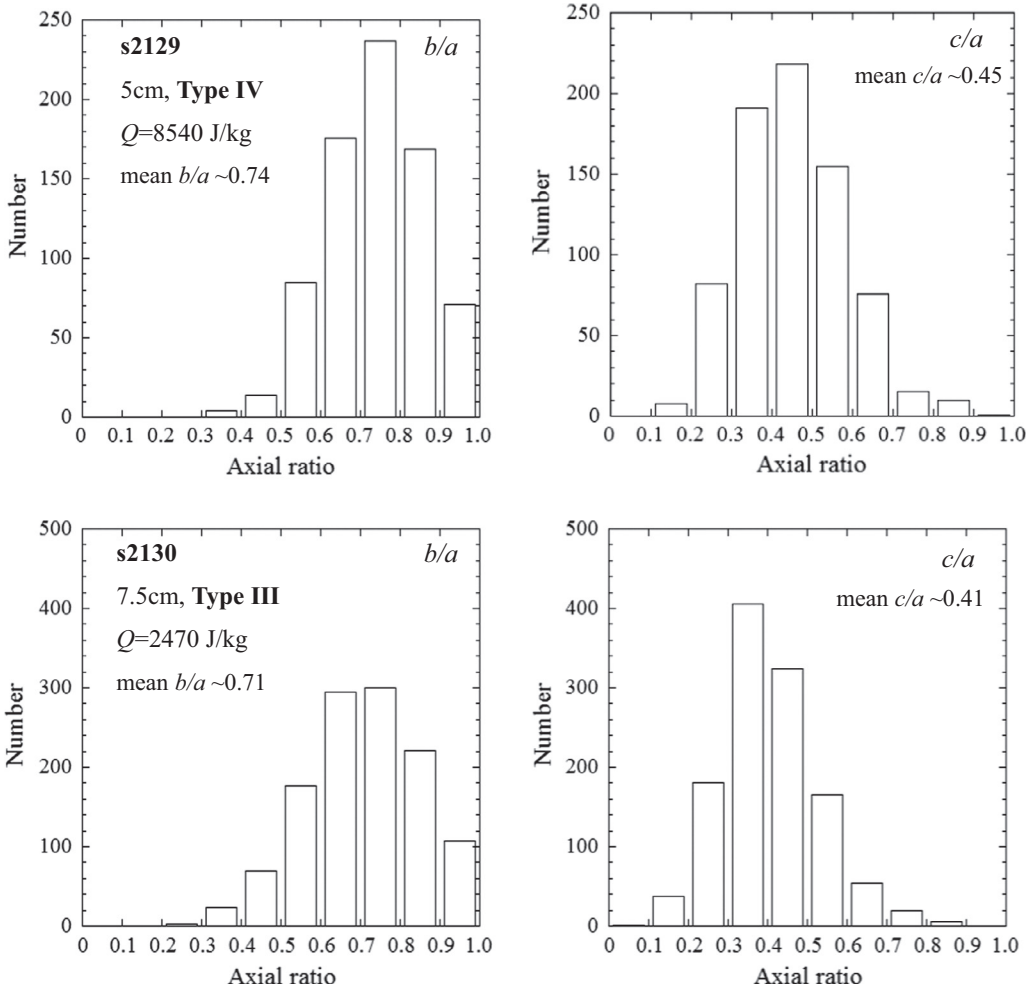

Fig. 6. A typical histogram for the shape distributions of fragments with $b \geqslant 4$ mm obtained from the cubic targets for the experiments in Fig. 5 (s2129, s2130, s2131, s2570 and s2572). Target sizes, fragmentation types, values of Q and mean b/a and c/a ratios are indicated.

3.2.3. Target shapes and fragment shapes

The data in Fig. 8 were acquired only for cubic targets. In Type I and II impacts, there are numerous flat fragments which are ejected from the target surface or near the target surface. The shape of the remaining largest fragment corresponded to the initial target without those parts of the side surface that had been chipped off. It is possible that the target shape influences the fragment shapes. Therefore, we conducted impact experiments on spherical, rectangular parallelepiped and slab targets with the same mass as our cubic target with 5 cm side length, and investigated the effect of target shape on fragment shape.

In the case of rectangular parallelepipeds and slabs, which have two wide and four narrow surfaces, it is possible that the area of the impact surface influences the fragment shape. Thus, two impact directions were adopted for these targets. One impact direction was parallel to the shortest axis of the target (s2421 and s2422), i.e. a projectile was shot into the target surface with the largest area. Another impact direction was parallel to the longest axis of the target (s2568 and s2569), i.e. a projectile was shot into the target surface with the smallest area. The impact point was the center of the target surface.

Fig. 9 indicates the histogram of shape distributions of the fragments with $b \geqslant 4$ mm for targets of various shapes. The general trend of these shape distributions is similar, except for the slab targets, although there are slight differences in the peak position. It is consistent with the experimental results of Durda et al. (2015), who used spherical and irregularly shaped targets. In slab targets, the proportion of flat fragments is rather high, and the mean c/a ratios are 0.36 (s2422) and 0.35 (s2569), less than the values in targets with different shapes ($c/a \sim 0.43$–0.46 for shots s2133, s2135, s2421 and s2568). We did not observe a significant dependence of b/a on the target shape ($b/a \sim 0.7$).

Fig. 10 shows the mass distribution of the fragments for the experiments shown in Fig. 9. In the cubic (s2133) and spherical (s2135) targets, as well as the rectangular parallelepiped (s2421) with the impact into the largest surface, the general trend of the mass distributions is similar. However, in rectangular parallelepipeds and slabs, the slopes of the mass distributions depend on impact direction. The slope of the mass distribution becomes less steep when the projectile is shot into the smallest surface of the target (s2568 and s2569). This means that there are fewer small fragments. There are only half as many fragments with $b \geqslant 4$ mm in s2568 and s2569 as there are in s2421 and s2422, respectively. Thus, the impact direction in these targets affects the mass distribution of the fragments. These variations may be caused by differences in the propagation of the impact energy in the target interior.

Comparing the shape and the mass distributions of the fragments, the exponent of the mass distribution does not seem to affect the shape distribution. For example, the mean c/a ratios for

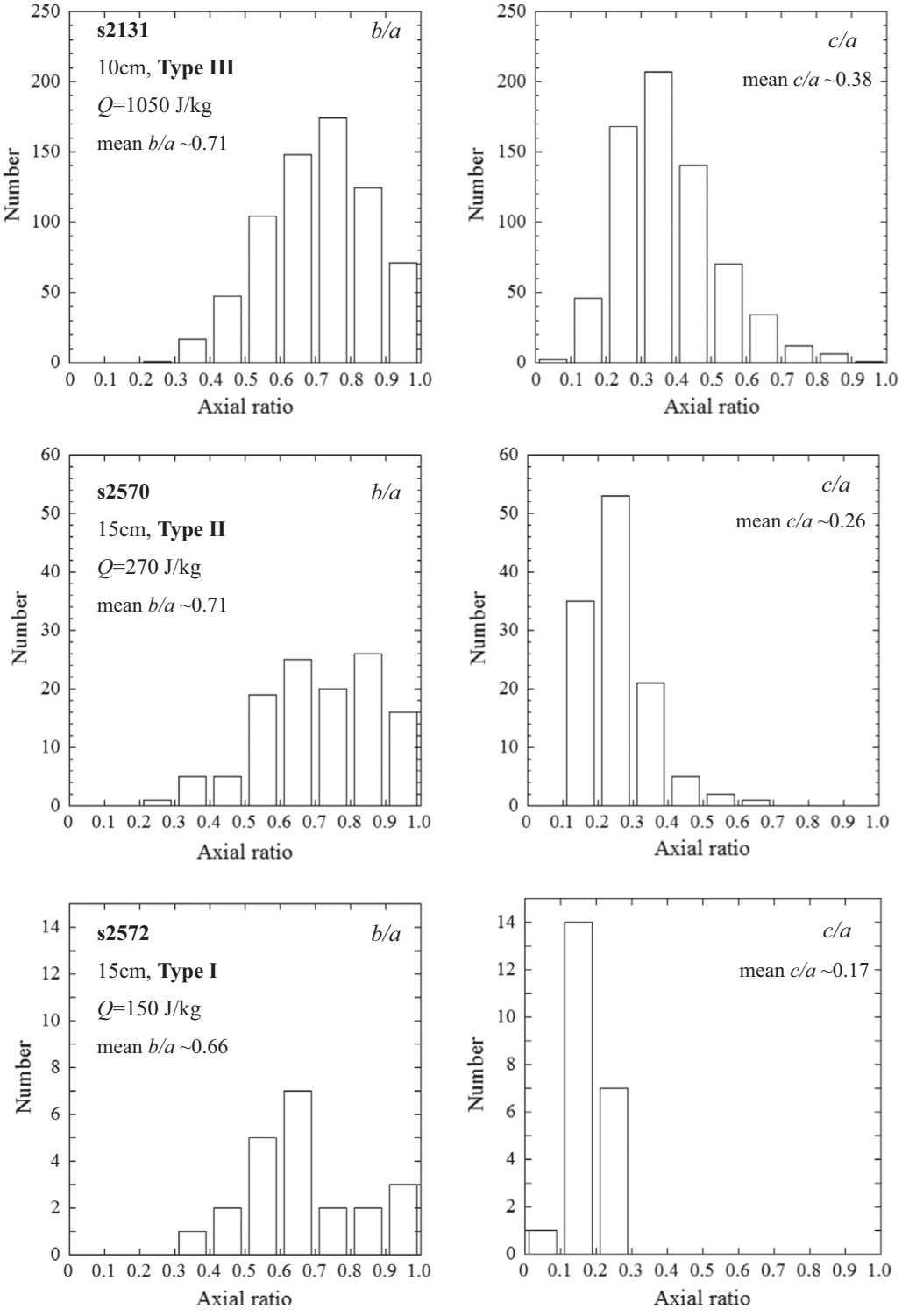

Fig. 6 (*continued*)

s2568 and s2422 are obviously different although the mass distributions for these experiments are not so different, and the mean *c*/*a* ratios for s2422 and s2569 are similar although the mass distributions for these experiments are obviously different. Thus, we could not find a relation between the exponent values in mass distributions and fragment shapes, as reported in Section 3.2.2.

In conclusion, the target shape does not influence the fragment shape except for slab targets, which is consist with the experimental observations of Durda et al. (2015). Besides, the data of slab targets would be of little relevance when applying the laboratory experiments to real collisions in space, because slab-like bodies have never been observed.

4. Discussion

4.1. Comparison with previous experiments

In the pioneering study of Fujiwara et al. (1978), cylindrical polycarbonate projectiles of mass 0.37 g were shot into cubic basalt targets of 5 cm (I1) and 5.2 cm (I2) side length at impact

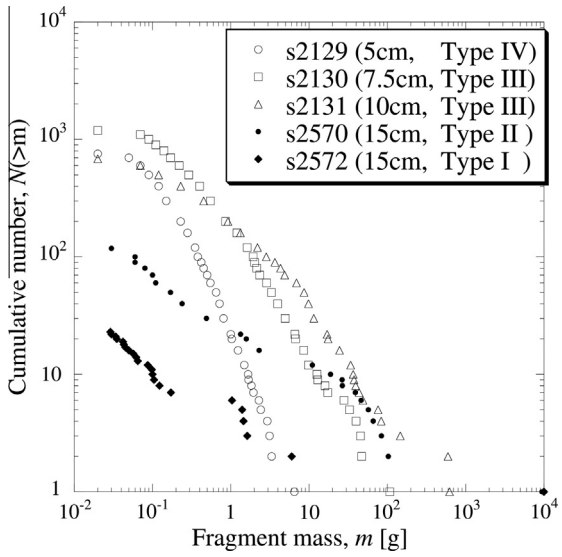

Fig. 7. Mass distributions of fragments for the experiments shown in Figs. 5 and 6 (s2129, s2130, s2131, s2570 and s2572). The collection ratios of the total mass of fragments with $b \geqslant 4$ mm to the initial target mass are 49% (s2129), 88% (s2130), 98% (s2131), 100% (s2570) and 100% (s2572), respectively. The collection ratio with $b \geqslant 4$ mm decreases with decreasing the target size (in response to increasing Q) while the recovery ratios of the total mass of all collected fragments (containing small fragments with $b < 4$ mm) to the initial target mass are more than 90%. For small fragments with less than 10 g, power law distributions are found with exponents $0.4 \leqslant \alpha \leqslant 1.1$ in the relationship $N(>m) = Am^{-\alpha}$ (where m is the fragment mass, α is the exponent, and A is the corresponding constant). The values of α are 1.1 (s2129), 0.8 (s2130), 0.5 (s2131), 0.5 (s2570) and 0.4 (s2572), respectively.

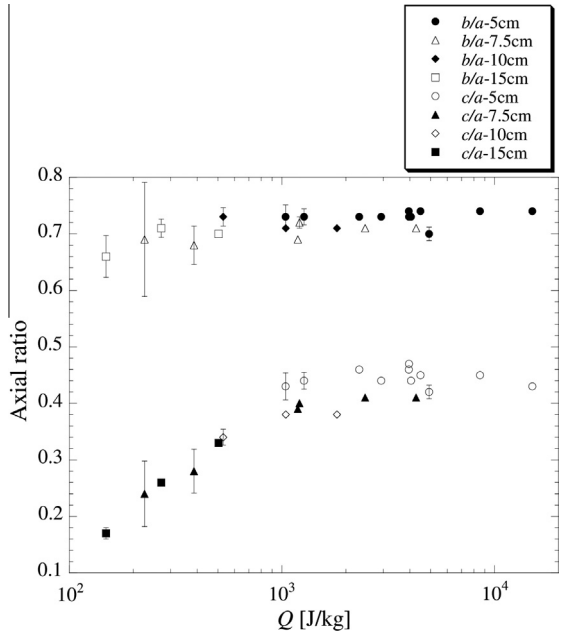

Fig. 8. The mean b/a and c/a ratios vs. Q. These data are for fragment shapes from the 23 impact experiments on cubic targets, and cover a wide range of Q (150–15,000 J/kg). The standard error bar of each shot is given. In the case of small (i.e. <0.01) standard errors, the error bar is smaller than the size of each symbol. The relatively large standard errors seen at small Q with less than 1000 J/kg are due to the small number of fragments with $b \geqslant 4$ mm. Note that the mean c/a ratios decrease with decreasing Q when Q is less than 1000 J/kg.

velocities of 2.6 km/s and 3.7 km/s, respectively. Both targets were catastrophically destroyed (core-type disruption), and the specific energies, Q, were 3700 J/kg for (I1) and 6700 J/kg for (I2). They estimated the mean axial ratios in those 719 fragments with $b > 4$ mm (I1 and I2) and found values of 0.73 for b/a and 0.50 for c/a. In the present study, for the experiments with $Q > \sim 3700$ J/kg we find that the mean b/a ratios lie in the range from 0.70 to 0.75 whilst the mean ratio c/a ratios lie between 0.41 and 0.47. These values are similar to those of Fujiwara et al. (1978), although our c/a values are slightly smaller. The trend that the mean c/a ratios are less than 0.50 has been found by other authors, too (e.g., Capaccioni et al., 1984, 1986; Giblin et al., 1994; Durda et al., 2015).

As one possible explanation for the above difference, La Spina and Paolicchi (1996) suggested that fragments with enough kinetic energy break again (secondary fragmentation) when they hit the interior surface of the small chamber, and secondary collisions affect the axial ratio of the fragments. This takes place preferentially along the longest axes, increasing the mean values of measured ratios. Fujiwara et al. (1978) used a relatively small chamber in their experiments. Therefore, their setup was not sufficiently tuned towards preventing destruction by secondary collisions of fast fragments, and the resulting values of c/a became larger.

In our experiments, we used a relatively large chamber and Styrofoam boards or urethane sheets, which should effectively prevent destruction by secondary collisions of fast fragments. Some images of the high-speed camera show that the fragments originating from the targets were not broken when they hit the Styrofoam boards or urethane sheets. In particular, our second series of setups used urethane sheets which should have prevented destruction by secondary collisions of fast fragments more effectively. For instance, the experimental results in Fig. 4 show 50–100 fewer fragments with $b \geqslant 4$ mm were created in s2415 (second setup) than in s2127, s2133 and s2134 (first setups). Besides, Fig. 3 shows that the mean c/a ratio for s2415 is smallest in these four experiments and the peak of the histogram in the axial ratio of c/a for s2415 shifts towards small values, which may mean that destructions by secondary collisions are rare.

The tendency for the mean c/a ratios to decrease in the case of weak disruption is compatible with the experimental results for ice targets at 257 K by Lange and Ahrens (1981). In addition to the experiments of Lange and Ahrens (1981), Durda et al. (2015) also reported that many thin, plate-like fragments are produced in the case of weak disruption (in their experiments, both irregularly-shaped and spherical basalt targets were investigate at impact speeds ranging from 3.6 to 5.8 km/s). For instance, when Q is 2240 J/kg (impact speed $\sim$ 3.7 km/s) in their experiments, the mean b/a and c/a ratios are 0.67 and 0.34, respectively. The values in their experiments are similar to those in non-catastrophic disruptions of our experiments, and their findings are partially consistent with ours. Unfortunately, the amount of their data is insufficient for developing a comprehensive model including small fragments, because they investigated only the 36 largest fragments from each shot of which six were fired. The measurement of more than 12,700 fragments in our experiments should be sufficient to reveal the relation between the fragment shape and the specific energy, Q.

Why do the mean c/a ratios decrease with decreasing Q when Q is less than 1000 J/kg? After the first few experiments, our suspicion was that the fragments with original target surfaces affect the mean c/a ratio. This is because, in Type I and II impacts (impact cratering or a small degree of fragmentation), almost all fragments originate from the surface and near-subsurface of the target. Thus, we investigated the fragment shapes with and without the original target surfaces (Fig. 11). The results show that, unexpectedly, the mean c/a ratios of fragments without original target surfaces are smaller than those with original target surfaces – except for the experiment with the smallest value of Q in Fig. 11. In other words, fragments without original target surfaces are flatter than those with original target surfaces. In the experiments, it is difficult to

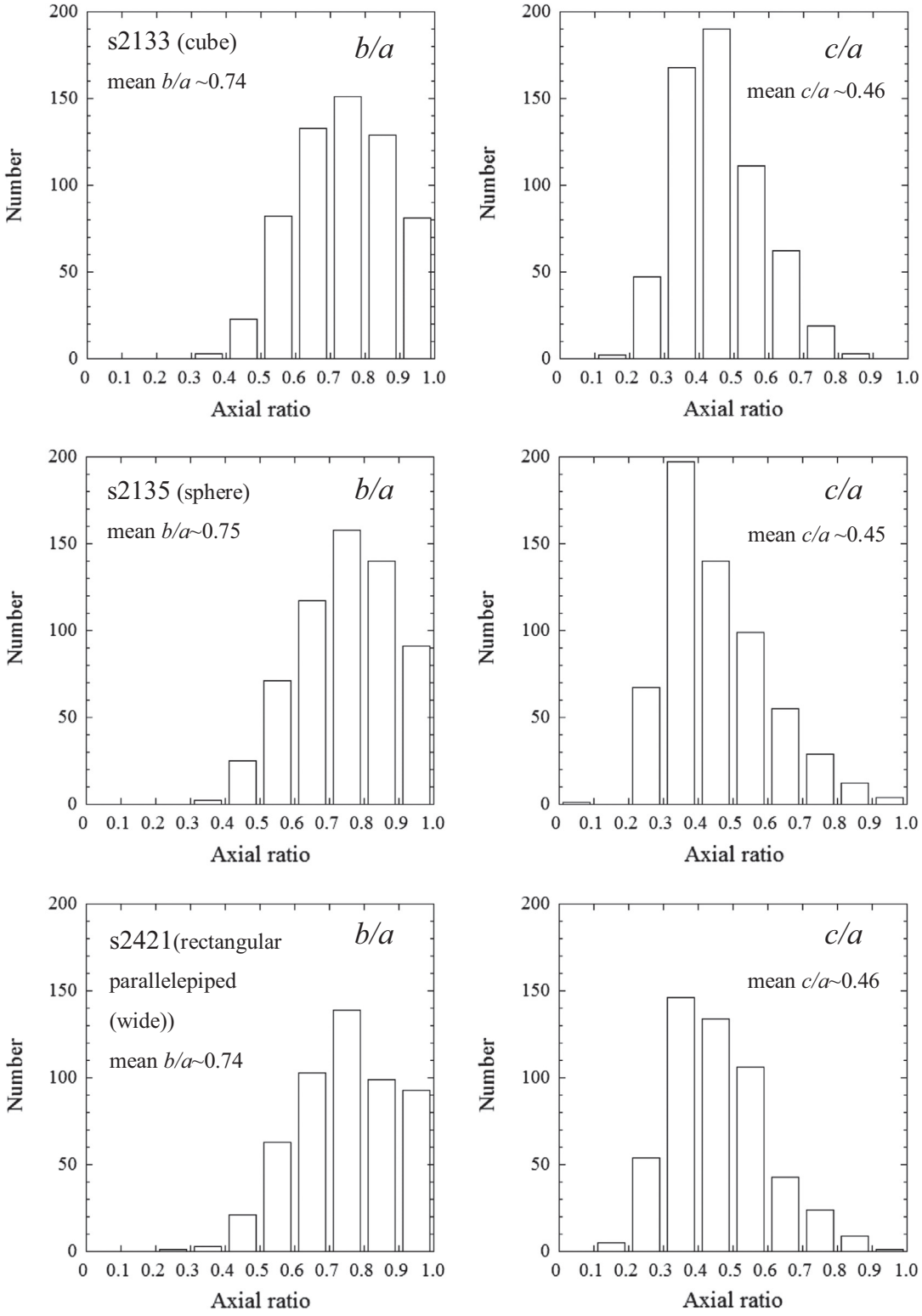

Fig. 9. Histograms for the shape distributions of fragments with $b \geqslant 4$ mm for targets of various shapes (one cube, one sphere, two rectangular parallelepipeds (2:1:1 side ratio) and two slabs (10:10:1 side ratio)), which all have the same mass as the cubic target with 5 cm side length. The mean b/a and c/a ratios are indicated. The two rectangular parallelepipeds and two slabs have two wide and four narrow surfaces. The corresponding impact surface of the projectile is given in parentheses. The impact velocities are around 3.5 km/s.

determine the positions of the fragments in the original target. However, high-speed camera images and the observation of the surface of the core (the largest fragment) would lead us to expect that many flatter fragments originate not only from the surface and subsurface of the target but also from the periphery of the core. A similar result was shown in the experiments of Durda et al. (2015). They described that many thin, plate-like fragments seem to have originated from the interior of the targets, near the core, in addition to the flattened fragments often seen to originate from the near-surface spall zone in cratering impacts. Further

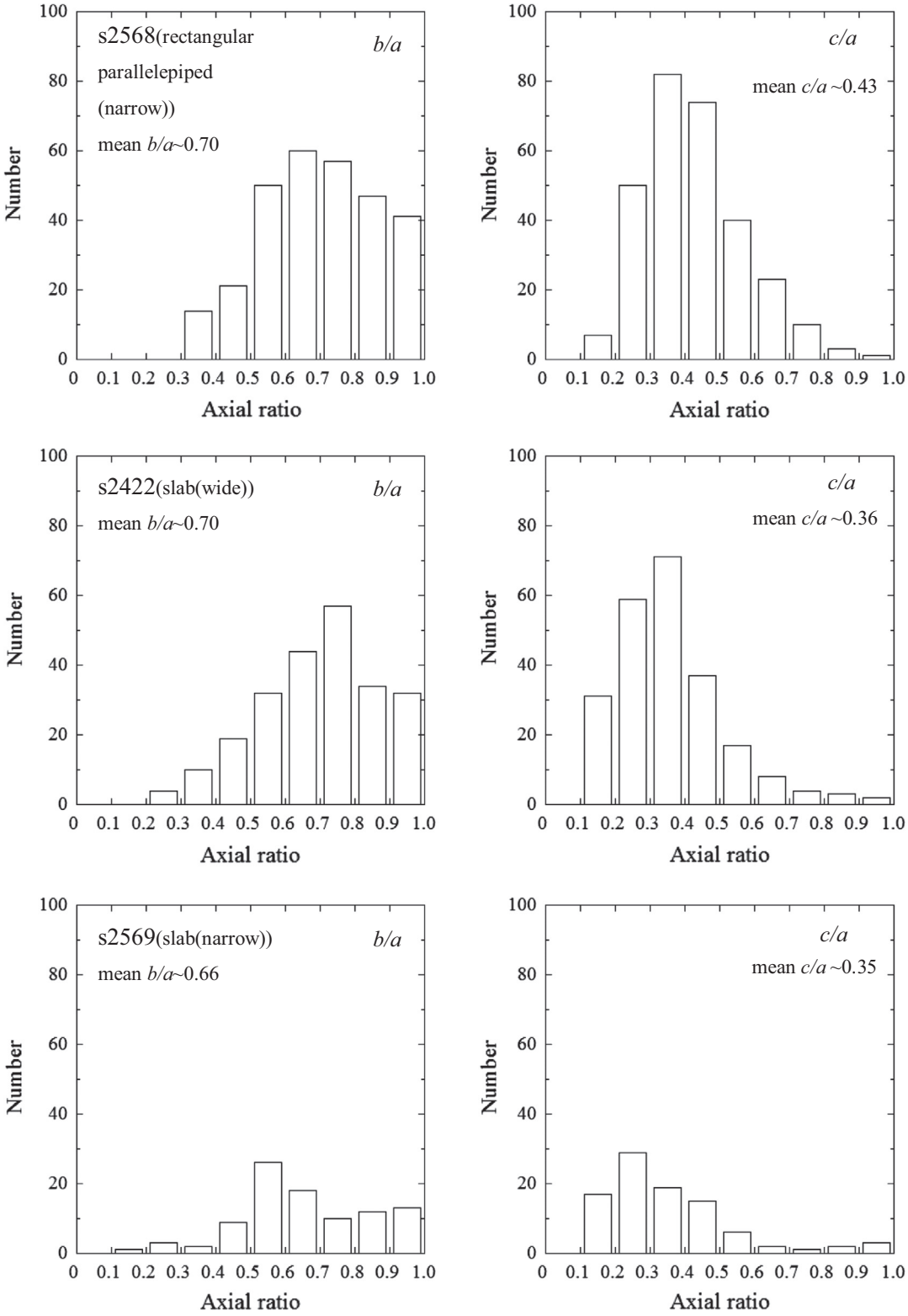

Fig. 9 (*continued*)

studies are necessary in order to understand why the mean *c*/*a* ratios decrease with decreasing *Q* when *Q* is less than 1000 J/kg.

4.2. Implication for asteroids

Although relating our laboratory experiments to collisions in space may not be straightforward, the data presented here can provide important evidence to interpret the shapes of asteroids and boulders on asteroid surfaces. As mentioned above, the shape distributions of some boulders on Asteroid Eros and the small- and fast-rotating asteroids with a diameter <200 m and a rotation period <1 h (which are considered to be monolithic) are similar to those of the laboratory fragments in catastrophic disruptions (Michikami et al., 2010). However, as pointed out by Holsapple

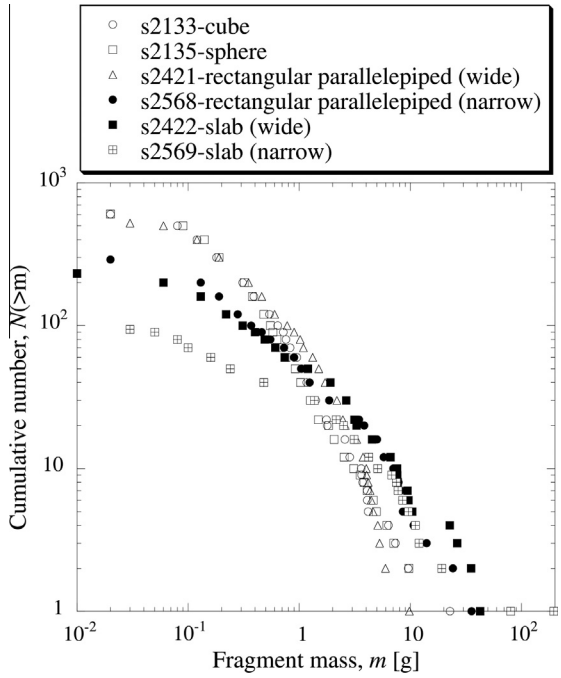

Fig. 10. Mass distributions of fragments for the experiments shown in Fig. 9. Targets are of various shapes.

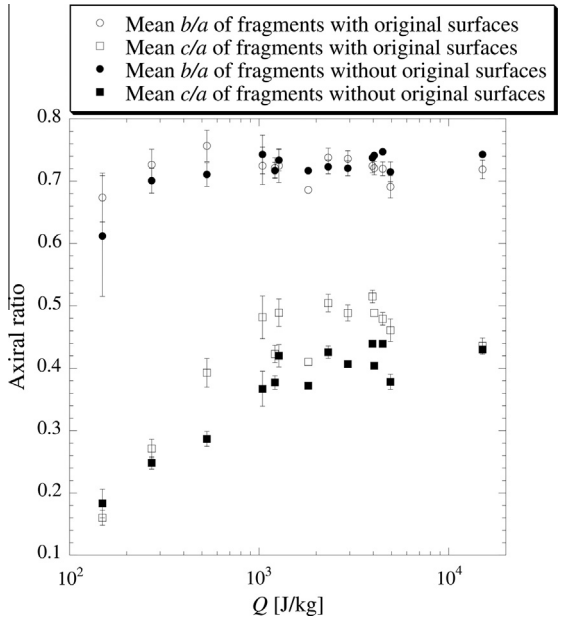

Fig. 11. The mean b/a and c/a ratios vs. Q for fragments with and without original target surfaces. These data are from 14 impact experiments into cubic targets, and cover a wide range of Q (150–15,000 J/kg). The figure does not show the data of further 9 impact experiments into cubic targets (s1934, s2126, s2128, s2129, s2130, s2131, s2132, s2133 and s2137), because these had already been carried out before a distinction between fragments with and without original target surfaces was deemed to be desirable. As there are more than 5700 fragments, a retroactive measurement is almost impossible.

et al. (2002), we must be cautious when extrapolating our data on fragment shapes from the laboratory to real asteroids, because monolithic asteroids are rare and the majority of asteroids are rubble piles.

In general, a rubble pile asteroid is macroscopically composed of a number of blocks. If each block were assumed to be a monolith, our data could be applied to a disruption phenomenon for a rubble pile asteroid. In the experiments, we found that the target shape does not largely influence the fragment shapes. Instead, the fragment shapes are strongly influenced by Q. If a rubble pile asteroid, consisting of several blocks, is broken by a meteoroid impact and each block experiences only a low Q, many fragments produced would have flat shapes (i.e. small c/a). To the contrary, if each block experiences a high Q, the fragments would have various shapes and the mean ratio of a:b:c would be close to 2:$\sqrt{}$2:1. In fact, the shape distributions of asteroids in young families are similar to those of the laboratory fragments in catastrophic disruption (Szabó and Kiss, 2008).

In addition to blocks, asteroid surfaces also consist of boulders. If boulders have experienced a catastrophic disruption in the parent body of the asteroid, the shape distribution of boulders should resemble that of the laboratory fragments in a catastrophic disruption. To confirm this, we take a look at the shapes of boulders on Itokawa's surface. This is because the investigation of the Itokawa particles on mineral chemistry suggested that Itokawa is an asteroid made of reassembled pieces (blocks and boulders) of the interior portions of a once $\geqslant$ 20 km sized asteroid (Nakamura et al. 2011). Besides, the appearance of Itokawa's surface and size of boulders shows that numerous boulders have been produced when Itokawa was generated by a catastrophic disruption of its parent body (e.g., Fujiwara et al., 2006; Saito et al., 2006; Michikami et al., 2008). We assumed that the heights of the boulders on the surface represent the c axes of the boulders. The dimensions of the c axes are first measured using several tens of home position images by the Hayabusa spacecraft (the distance between the spacecraft and Itokawa is 20 km). The dimensions of the a and b axes of the boulders are derived from the images which rotated by 90° with respect to the image used for determining c. As a result, the mean b/a and c/a ratios for 21 arbitrarily selected boulders $\geqslant$ 8 m are 0.66 and 0.46, respectively. Recalling the results of our experiments outlined above, these shapes are similar to those of the fragments in our catastrophic disruption experiments, which implies that the parent body of Itokawa is likely to have experienced a catastrophic disruption rather than a weak disruption. These results confirm the conclusions drawn from the mineral chemistry of the Itokawa particles (Nakamura et al., 2011) and the geography of the Itokawa surface (e.g., Fujiwara et al., 2006; Saito et al., 2006; Michikami et al., 2008).

5. Conclusions

We have systematically investigated the fragment shapes created in impacts in the range from cratering to catastrophic disruption. Impact experiments for basalt targets 5–15 cm in size were performed using a two-stage light-gas gun at ISAS, JAXA. The target bulk density was 3000 kg/m^3, the compressive strength was 185 MPa, and the tensile strength was 14 MPa. A spherical nylon projectile with 7.14 mm in diameter was shot perpendicularly into the target surface at velocities of 1.6–7.0 km/s. In a total of 28 impact experiments we have measured more than 12,700 fragments with $b \geqslant 4$ mm with digital calipers. In the present study, fragment shape is defined by the ratios b/a and c/a, where a, b and c are defined as the dimensions of a fragment in three mutually orthogonal planes ($a \geqslant b \geqslant c$).

In order to investigate the dependence of fragment shape on the degree of fragmentation, the mean axial ratios of the fragment shapes in each shot were plotted against the specific energy Q, which is defined as the kinetic energy of the projectile per unit target mass. The results show that the mean b/a ratios seem to be

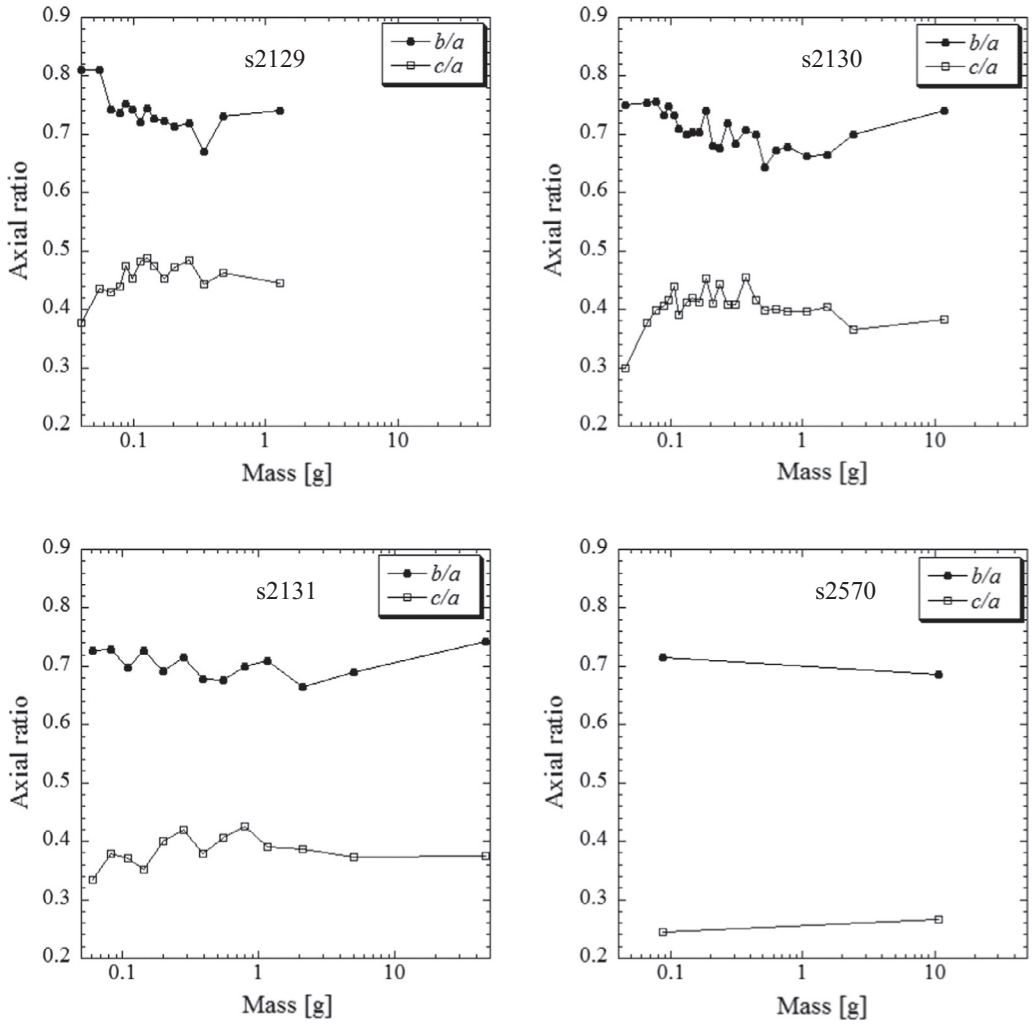

Fig. A1. Running box diagram of the mean b/a and c/a ratios in each bin including 50 fragments vs the fragment mean mass, which are the same data presented in Figs. 5–7, except for shot s2572. In s2570, the mean b/a and c/a ratios do not contain the largest fragment whose mass is roughly the same as initial target mass.

roughly constant, or seem to slightly decrease with decreasing Q. On the other hand, although the mean c/a ratios seem to be roughly constant when $Q \geqslant 1000$ J/kg, they decrease gradually with decreasing Q when $Q < 1000$ J/kg. There are more flat fragments when the degree of fragmentation is small (i.e. in non-catastrophic disruptions). This trend has not been found in previous experiments. For example, the mean c/a ratio in an impact cratering event is nearly 0.2, which is considerably smaller than c/a in a catastrophic disruption (~0.5). In addition, the effect of target shape on fragment shape was investigated. We carried out the impact experiments for one spherical, two rectangular parallelepiped and two slab targets with the same mass as our cubic target with 5 cm side length. The impact velocities were approximately 3.5 km/s. The results indicate that the target shape does not influence the fragment shape except for slab targets.

Although relating our laboratory experiments to collisions in space may not be straightforward, the data presented here can provide important evidence to interpret the shapes of asteroids and boulders on asteroid surfaces. The shapes of 21 arbitrarily selected boulders ($\geqslant$ 8 m) on Asteroid Itokawa were researched using several tens of images taken by the Hayabusa spacecraft. The mean c/a value of these boulders is 0.46, which is similar to our experimental value for catastrophic disruption. This implies that the parent body of Itokawa could have experienced a catastrophic disruption rather than a weak disruption. Investigations of the mineral chemistry of the Itokawa particles collected by Hayabusa suggest that Itokawa is an asteroid made of reassembled pieces of the interior portions of a once $\geqslant$ 20 km sized asteroid. The same conclusion was obtained from the appearance of Itokawa's surface and size of boulders. Our experimental result supports this conclusion. Our investigations of fragment shape have thus helped constrain current interpretations of asteroid formation.

Acknowledgments

The authors acknowledge H. Tanaka and M. Ogawa for the support of their experiments. We also thank the staff members at the symposium for impacts at the Institute of Low temperature Science, Hokkaido University, who provided useful discussions and suggestions. We would also like to acknowledge financial support from the UK's STFC under Grant No. ST/L000776/1. This paper was significantly improved by the comments from anonymous reviewers. A. Tsuchiyama was supported by a Grant-in-Aid of the Japan Ministry of Education, Culture, Sports, Science and Technology (19104012). The experiments described in this paper were conducted and supported by ISAS/JAXA in collaboration with the Space Plasma Laboratory (the Hypervelocity Impact Facility).

Appendix A. Fragment mass and fragment shapes

Previous experiments indicate that the fragment shapes do not depend on the fragment mass (e.g., Capaccioni et al., 1986). To confirm this, the effect of the fragment mass on fragment shapes is investigated using the same data from Figs. 5–7 with the exception of shot s2572 (Fig. A1). We have plotted a running-box diagram of the mean axial ratios vs the fragment mean masses. The fragments have been ordered by mass and grouped into bins of 50 fragments each. At smaller mass there seems to be more fluctuation than at larger mass, which merely reflects the fact that there are numerous small fragments at smaller mass, and fewer large fragments at larger mass. As a whole, no significant difference of the mean axial ratio is apparent. However, we do not rule out that the fragment mass influences the fragment shape because the mean axial ratios of b/a and c/a in Fig. A1 seem to have a lower limit and an upper limit in the intermediate mass range, respectively. The lower and upper limits may point at physical processes during the impact. It is, however, difficult to speculate on the reasons because the data in mass cover only two orders of magnitude and the existences of the lower and upper limits in several orders of magnitude are unclear. A quantitative investigation for the effect of fragment mass on the fragment shape would be needed in the future, analyzing the data in mass with several orders of magnitude.

References

Bianchi, R. et al., 1984. Experimental simulation of asteroidal fragmentation by macroscopic hypervelocity impacts against free falling bodies. Astron. Astrophys. 139, 1–6.

Capaccioni, F. et al., 1984. Shapes of asteroids compared with fragments from hypervelocity impact experiments. Nature 308, 832–834.

Capaccioni, F. et al., 1986. Asteroidal catastrophic collisions simulated by hypervelocity impact experiments. Icarus 66, 487–514.

Durda, D.D. et al., 2015. The shapes of fragments from catastrophic disruption events: Effects of target shape and impact speed. Planet. Space Sci. 107, 77–83.

Fujiwara, A., Kamimoto, G., Tsukamoto, A., 1977. Destruction of basaltic bodies by high-velocity impact. Icarus 31, 277–288.

Fujiwara, A., Kamimoto, G., Tsukamoto, A., 1978. Expected shape distribution of asteroids obtained from laboratory impact experiments. Nature 272, 602–603.

Fujiwara, A. et al., 2006. The rubble–pile Asteroid Itokawa as observed by Hayabusa. Science 312, 1330–1334.

Giblin, I. et al., 1994. Field fragmentation of macroscopic targets simulating asteroidal catastrophic collisions. Icarus 110, 203–224.

Holsapple, K. et al., 2002. Asteroid impacts: Laboratory experiments and scaling laws. In: Bottke, W.F., Cellino, A., Paolicchi, P., Binzel, R.P. (Eds.), Asteroids III. University of Arizona Press, Tucson, pp. 443–462.

La Spina, A., Paolicchi, P., 1996. Catastrophic fragmentation as a stochastic process: Sizes and shapes of fragments. Planet. Space Sci. 44, 1563–1578.

Lange, M.A., Ahrens, T.J., 1981. Fragmentation of ice by low-velocity impact. In: Proceedings of the 12th Lunar Planetary Science Conference, pp. 1667–1687.

Matsui, T. et al., 1982. Laboratory simulation of planetesimal collisions. J. Geophys. Res. 87, 10968–10982.

Matsui, T., Waza, T., Kani, K., 1984. Destruction of rocks by low velocity impact and its implications for accretion and fragmentation processes of planetesimals. J. Geophys. Res. Suppl. 89, B700–B706.

Medvedev, R.V., Gorbatsevich, F.I., Zotkin, I.T., 1985. Determination of the physical properties of stony meteorites with application to the study of processes of their destruction. Meteoritika 44, 105–110 (in Russian).

Michikami, T. et al., 2008. Size–frequency statistics of boulders on global surface of Asteroid 25143 Itokawa. Earth Planets Space 60, 13–20.

Michikami, T., Nakamura, A., Hirata, N., 2010. The shape distribution of boulders on Asteroid 25143 Itokawa: Comparison with fragments from impact experiments. Icarus 207, 277–284.

Nakamura, T. et al., 2011. Itokawa dust particles: A direct link between S-type asteroids and ordinary chondrites. Science 333, 1113–1116.

O'Brien, D.P., Greenberg, R., 2005. The collisional and dynamical evolution of the main-belt and NEA size distributions. Icarus 178, 179–212.

Ryan, E.V., Davis, D.R., 1994. Asteroid collisions: The impact disruption of cooled iron meteorites. American Astronomical Society, DPS Meeting #26, #31.10. Bull. Am. Astron. Soc. 26, 1180.

Saito, J. et al., 2006. Detailed images of Asteroid 25143 Itokawa from Hayabusa. Science 312, 1341–1344.

Szabó, G.M., Kiss, L.L., 2008. The shape distribution of asteroid families: Evidence for evolution driven by small impacts. Icarus 196, 135–143.

Takagi, Y., Mizutani, H., Kawakami, S., 1984. Impact fragmentation experiments of basalts and pyrophyllites. Icarus 59, 462–477.

Zappalà, V. et al., 1995. Asteroid families: Search of a 12,487-asteroid sample using two different clustering techniques. Icarus 116, 291–314.